

Release of simulated data

Generating mock catalogs with Gencat

INAF – OAR for the Astrodeep project



ASTRODEEP

"Unveiling the power of the deepest images of the Universe"

THEME [SPA.2012.2.1-01]

[Exploitation of space science and exploration data]

Grant agreement for: Collaborative project

Grant agreement no: 312725

ABSTRACT

In this document we present the tool that was developed by the Astrodeep collaboration for the creation of simulated images. This set of simulated images, reproduces the expected data from Hershel and other satellites and telescopes. This dataset has been used to define and test the software tools and methods described in Deliverables D3.3 and D3.4.

Deliverable Number D3.2 – Delivery date June 2015.

*Prepared by: D. Elbaz, C. Schreiber, E. Merlin, A. Fontana
Approved by: AEC
Date: 05/06/2015*

Generating mock catalogs with gencat

1 Introduction

Up until now we have been using the *SkyMaker*¹ program (E. Bertin) to produce realistic high resolution images, which we regularly use to test the various source extraction methods and algorithms we are developing within Astrodeep. In input, this program requires a simulated galaxy catalog, which is produced by the *Stuff*² program (also created by E. Bertin).

The quality of these simulated catalogs is not optimal. In particular, the distribution of the simulated fluxes in some bands differ substantially from those that are observed, leading to simulated images that are not representative of the real products we are working on. Unfortunately, both *SkyMaker* and *Stuff* are poorly documented, and we cannot easily remedy to this problem. For this reason, we have developed a new tool to generate simulated galaxy catalog, called *gencat*³. The main ideas behind the procedure are summarized in Section 2.

This new tool can generate catalogs in the format required by *Sky Maker*, and therefore can be used as a “drop-in” replacement for *Stuff*. Using this tool we are able not only to generate fluxes in all the photometric bands from 3000 Å to 8 μm, like *Stuff*, but we also merge in our technique to simulate far-IR fluxes from 8 μm to 3 mm, essentially covering, in a single tool, the whole wavelength range where stellar and dust emission dominate.

Finally, the quality of the generated catalogs has greatly improved compared to original catalogs built with *Stuff*. As can be seen in Section 3, we are able to produce flux distributions in all the bands which are indistinguishable from the real, observed flux distributions. The simulated images, both at *Hubble* and *Herschel*-like resolution, have very good statistical properties. This will allow us to perform more accurate tests of our methods, and also to deliver high quality simulations to the community.

2 Creating the mock catalog

The main idea behind the generation process of this mock catalog is that everything can be statistically inferred from the redshift, the stellar mass and the “star-forming” flag of each galaxy. The procedure is therefore composed of two main steps: first, generate a realistic distribution of masses at different redshifts both for active and passive galaxies using observed mass-functions; second, estimate all the other physical properties using statistical recipes calibrated on the observed galaxies: morphology, SFR, attenuation, optical colors, and sky-projected position.

2.1 Generating redshifts and masses

The purpose of the mock catalog is the simulate a field similar to the GOODS–South CANDELS field. Therefore, in order to most closely mimic the properties of this field, we use the conditional mass functions at different redshifts which are described in Schreiber et al. (2015). Briefly, the whole GOODS–South catalog is cut at $H < 26$ to ensure high completeness, split in two population of “active” and “passive” galaxies according to the UVJ color-color selection, and further split in multiple redshift bins from $z = 0.3$ to $z = 4.5$. These redshifts and stellar masses have been computed by Maurilio Pannella with EAZY and FAST, respectively, on the official CANDELS photometry. We then computed the mass distribution of each of these sub-samples, performing first order completeness corrections, and fit a double Schechter law. Using these fits, we can generate mass functions down to arbitrarily low stellar masses. To reach higher redshifts, we have used the mass functions calculated by Grazian et al. (2015)

¹<http://www.astromatic.net/software/skymaker>

²<http://www.astromatic.net/software/stuff>

³<https://github.com/cschreib/gencat>

for $z < 7.5$. The $z = 0$ mass function is adapted from Baldry et al. (2012), but it should not matter much for now since we are aiming for pencil-beam surveys which contain very few local galaxies.

Once this is done, we define a fine grid of redshifts, e.g. from $z = 0.01$ to $z = 6$, and choose the sky area of the mock catalog. For now we work with an area similar to the first catalog produced with Stuff, i.e. 17×17 arcmin. Then for each element of the redshift grid, we use the mass functions to generate a sample of stellar masses. The minimum stellar mass M_{\min} can be chosen either to be constant (e.g. $10^7 M_{\odot}$) or to vary with redshift so as to reach a given magnitude limit in the selection band, for example $H < 27$. This requires using the optical SED library described below to obtain a rough estimate of the mass completeness.

At this stage, the mock catalog has exactly the same mass and redshift distribution as the CANDELS catalog in GOODS–South. This is a good thing to ensure a high fidelity of the simulated catalog, but one has to keep in mind that, by construction, this also means that we have imposed the same cosmic variance than in the real GOODS–South field.

2.2 Generating morphology

The Stuff program was not only generating photometry, but also detailed morphology in each band. In particular, each galaxy is assumed to be composed of two component: a bulge (de Vaucouleur profile, Sérsic $n = 4$) and a disk (exponential profile, Sérsic $n = 1$). In order to be able to plug this new mock catalog in *SkyMaker* directly, we also need to generate these informations.

The first important quantity is the bulge-to-total ratio B/T , which tells what fraction of the total mass of the galaxy goes into the bulge, as opposed to the disk. We generate this quantity using the relations between B/T and M_* published by Lang et al. (2014). These relations are conveniently provided both for active and passive galaxies, at different redshifts. They report no strong redshift evolution between $z = 1$ and $z = 2$, so we chose to make the B/T simply depend on mass following

$$(B/T)_{\text{active}} = 0.2 \times \left(\frac{M_*}{10^{10}} \right)^{0.27} \times 10^{G(0.2)} \text{ and} \quad (1)$$

$$(B/T)_{\text{passive}} = 0.5 \times \left(\frac{M_*}{10^{10}} \right)^{0.1} \times 10^{G(0.2)}, \quad (2)$$

where $G(\sigma)$ is a zero-mean Gaussian noise of amplitude σ . The B/T is then clamped to $0 \leq B/T \leq 1$. This quantity will also be used later to define the colors of the galaxies.

The other set of morphological properties we need to generate are the axis ratio, position angle and size of both the disk and the bulge component of each galaxy. We chose to give the same position angle to both components (which is the average trend observed in the morphological catalogs of Simard et al. 2011 for galaxies in the SDSS), and chose it randomly with uniform probability between -90 deg and $+90$ deg.

The axis ratio is generated following the distribution observed in the real catalogs: for the disk (resp. bulge), we built a sample of galaxies with Sérsic index $n < 1.5$ (resp. $n > 2.5$) and computed their axis ratio distribution (Sérsic indices were computed by van der Wel et al. 2014). The result is shown in Fig. 1. As expected, disks-dominated galaxies (blue) are found to be more elongated than bulge-dominated galaxies (red).

To estimate the sizes, we used the same sub-samples as above, and looked at the relation between the observed H -band size, mass, and redshift. We could parametrize the observed relations and their scatter with the following formula

$$R_{\text{disk}} = \begin{cases} (1+z)^{-1.25} \times \left(\frac{M_*}{10^{10}} \right)^{0.17} \times 10^{G(0.2)} & \text{for } z < 1.5, \\ 0.4 \times (1+z)^{-0.25} \times \left(\frac{M_*}{10^{10}} \right)^{0.17} \times 10^{G(0.2)} & \text{for } z > 1.5, \text{ and} \end{cases} \quad (3)$$

$$R_{\text{bulge}} = (1+z)^{-2.5} \times \left(\frac{M_*}{10^{10}} \right)^{0.7} \times 10^{G(0.2)}, \quad (4)$$

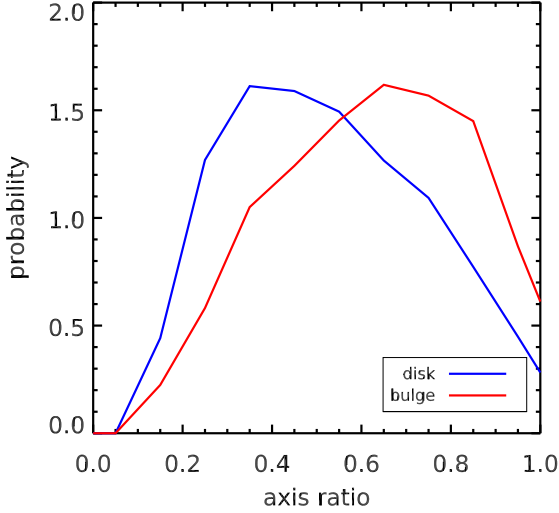


Figure 1: Observed axis ratio distribution of disk-dominated ($n < 1.5$) and bulge-dominated ($n > 2.5$) galaxies. Sérsic fits were taken from the CANDELS wiki, and were produced by Arjen van der Wel. Note that we also added a cut in stellar mass, in order not to be polluted by low mass faint galaxies ($M_* > 10^9 M_\odot$ for disks, $M_* > 3 \times 10^{10} M_\odot$ for bulges).

2.3 Generating star formation rate

To generate star formation rates (SFRs), we used the Main Sequence approach, which attributes a “main sequence” SFR to every galaxy, knowing its redshift and its stellar mass. We used the calibration published in Schreiber et al. (2015), Eq. 9. On top of this, a random lognormal scatter of 0.3 dex is added, and a small fraction (3.3%) of the sample is randomly put in the “starburst” mode, following the 2SFM model (Sargent et al. 2012), and using the best-fit parameters obtained in Schreiber et al. (2015). In the end:

$$R_{\text{SB}} = \begin{cases} 10^{G(0.3)} & \text{for Main Sequence galaxies} \\ 5.2 \times 10^{G(0.3)} & \text{for Starburst galaxies} \end{cases} \quad (5)$$

$$\text{SFR} = \text{SFR}_{\text{MS}} \times R_{\text{SB}}. \quad (6)$$

This quantity, R_{SB} , the “starburstiness”, is used later to generate the IR photometry.

Then, we split this SFR between obscured and non-obscured components. The obscured component generates the IR fluxes, while the non-obscured component emerges naturally in the UV. To do so, we use the evolution of $\text{IRX} \equiv L_{\text{IR}}/L_{\text{UV}}$ observed in the *Herschel* stacks of Schreiber et al. (2015) (see also Heinis et al. 2014), which gives

$$\text{IRX} = \frac{L_{\text{IR}}}{L_{\text{UV}}} = \begin{cases} 15.8 \times \left(\frac{M_*}{3 \times 10^{10}}\right)^{0.45z+0.35} & \text{for } z < 3 \\ 15.8 \times \left(\frac{M_*}{3 \times 10^{10}}\right)^{1.7} & \text{for } z > 3. \end{cases} \quad (7)$$

From there it is then simple to recover L_{IR} and L_{UV} , and therefore the obscured and non-obscured part of the SFR. Passive galaxies are given zero SFR.

2.4 Generating optical colors

To generate UV to near-IR fluxes, we first need to choose an optical SED for each galaxy. To do so, we choose to start from the *UVJ* color-color diagram. In this diagram, passive galaxies occupy a well defined region (red cloud), while star-forming galaxies form a “sequence”, which is actually generated by a combination of attenuation and age (see e.g. Williams et al. 2009, Fig. 8). This is useful, because it is known that both age and attenuation (e.g. Pannella et al. 2014) correlate strongly with the stellar mass. We used this fact to create a simple recipe to associate colors to active and passive galaxies, knowing only their redshift and masses.

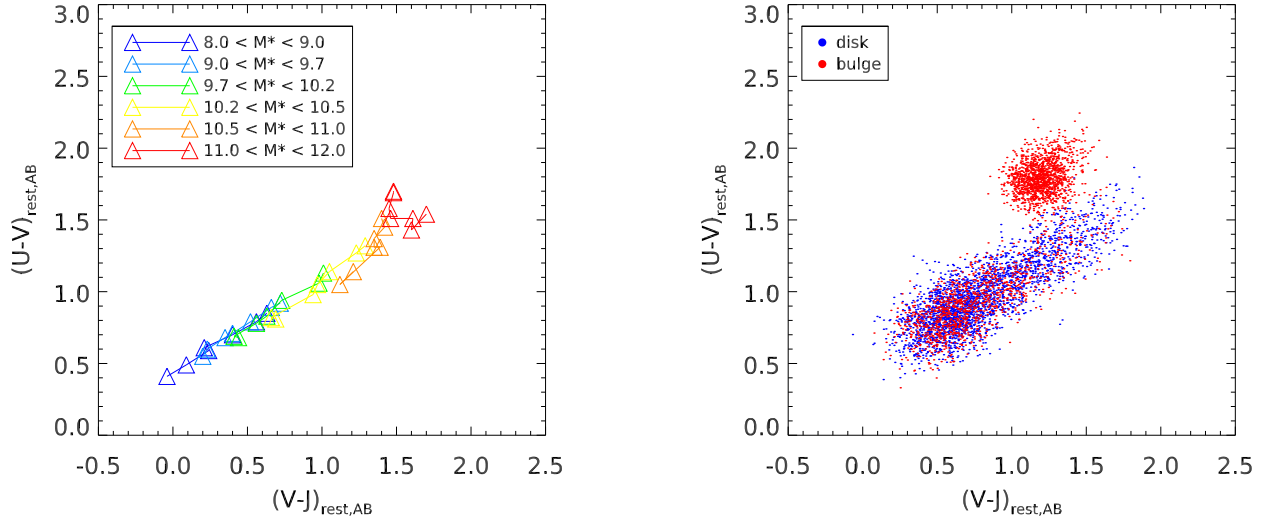


Figure 2: **Left:** Observed median colors of galaxies of different masses, for different redshift (from $z = 0.3$ to $z = 3.0$). The trend is that galaxies move diagonally toward the bottom-left corner when going to higher redshifts. **Right:** Generated UVJ colors of disk (blue) and bulge (red) components of galaxies with $M_* > 10^9 M_\odot$ and $0.8 < z < 1.2$.

We find that passive galaxies are well condensed in a fixed region, close to $V - J = 1.25$ and $U - V = 1.85$, with a very small trend with stellar mass. The principle is to put all passive galaxies at this position, shift them along the attenuation vector direction according to their stellar mass, and add some Gaussian noise to the generated colors. The final colors are chosen following

$$A = 0.1 \times (\log_{10}(M_*/M_\odot) - 11) + G(0.1), \quad (8)$$

$$(V - J)_{\text{passive}} = 1.25 + A + G(0.1), \quad (9)$$

$$(U - V)_{\text{passive}} = 1.85 + 0.88 \times A + G(0.1). \quad (10)$$

Note that the “shift” A is clamped to the range $[-0.1, 0.2]$ so that galaxies do not leave the red cloud.

For star-forming galaxies, one needs to be a bit more subtle because their colors vary a lot more. As can be seen, e.g., in Fig. 1 from Schreiber et al. (2015), star-forming galaxies populate different regions of the UVJ diagram depending on the stellar mass and redshift: massive galaxies are preferentially located on the top-right corner (red $U - V$ and $V - J$ colors), while low-mass galaxies are at the bottom-left (blue in $U - V$ and $V - J$), and they are shifted to bluer colors at higher redshift. We can parametrize this evolution.

To do so, we took a sample of UVJ star-forming galaxies in GOODS–South, and split them in mass bins. We further decompose each of these bins by slicing in redshift, and compute the median $U - V$ and $V - J$ colors. This produces a set of tracks in the UVJ diagram, which are reproduced in Fig. 2 (left). It turns out that these tracks fall roughly on a fixed line of slope 0.65, so reproducing these trend is relatively easy. We end up with the following formula

$$A_0 = 0.58 \times \text{erf}(\log_{10}(M_*/M_\odot) - 10) + 1.39, \quad (11)$$

$$A_s = \begin{cases} -0.34 + 0.3 \times \log_{10}\left(\frac{M_*}{2.2 \times 10^{10} M_\odot}\right) & \text{for } M_* > 2.2 \times 10^{10} M_\odot, \\ -0.34 & \text{for } M_* < 2.2 \times 10^{10} M_\odot, \end{cases} \quad (12)$$

$$(13)$$

$$A_1 = A_0 + A_s \times z, \quad (14)$$

$$A = A_1 + G(0.1), \quad (15)$$

$$(V - J)_{\text{active}} = 0.0 + A \times \cos(\theta) + G(0.12), \quad (16)$$

$$(U - V)_{\text{active}} = 0.45 + A \times \sin(\theta) + G(0.12). \quad (17)$$

with A_1 being limited to at most 2, and $\theta = \arctan(0.65)$.

This parametrization will generate a UVJ diagram very similar to the observed one, with the same redshift and mass trends. However, the observed UVJ diagram is made out of the *total* light of the galaxy: here we need to decompose the galaxy into a bulge and a disk component, and both have usually different colors. The way we chose to handle this issue is to always use the “active” UVJ colors for disk components, always use the “passive” UVJ colors for bulges of bulge-dominated galaxies ($B/T > 0.6$), and randomly use either the “passive” or the “active” UVJ colors for the bulges of intermediate galaxies ($B/T < 0.6$) with 50% probability each. These prescriptions are lacking any direct observational constraints, and were therefore chosen somewhat arbitrarily so as to both reflect intuition and reproduce the observed color distribution.

The resulting UVJ colors are shown in Fig. 2 (right).

2.5 Choosing an optical SED

We then use these colors to associate a full optical SED to the galaxies. The idea is to consider that there is an average SED at each position on the UVJ diagram, and that one can attribute this average SED to the galaxies that are located at this position.

Therefore we have binned the UVJ plane into small buckets of about 0.1 mag, and computed the observed average rest-frame SED of all the galaxies that fall inside each bucket, assuming no redshift dependence. These rest-frame SEDs are actually generated by FAST with Bruzual & Charlot (2003) stellar population models, assuming a delayed exponentially declining star formation history. The result is a wide library of about 850 reference SEDs, all normalized per unit stellar mass.

Then the procedure is simply to pick one of these SEDs depending on the position of the galaxy in the UVJ diagram. We run this procedure for both disk and bulge components, multiply the chosen SEDs by the respective stellar mass of each component, redshift them to the redshift of the galaxy, and finally integrate the resulting SED over the chosen UV-NIR passbands to generate the corresponding fluxes.

2.6 Choosing an IR SED

The generation of the IR fluxes is the same as the one we used to generate the *Herschel* images with the previous Astrodeep mock catalog. Basically, we use the Chary & Elbaz (2001) library of FIR SEDs, normalize them to unit L_{IR} , and attribute one of these SEDs to every galaxy, from its redshift and “starburtiness” (see Section 2.3). At higher redshifts, galaxies have warmer dust temperatures (Magdis et al. 2012), and the dust temperature also correlates with the offset of a galaxy from the Main Sequence (Magnelli et al. 2014). We use here the redshift evolution that was observed in the stacked *Herschel* SEDs of Schreiber et al. (2015).

Then, as for the optical flux computation, the chosen SED is multiplied by the L_{IR} of the galaxy, redshifted, and integrated over the chosen IR passbands to produce the final fluxes. For simplicity, we chose to attribute all of the FIR flux to the “disk” component. This should not matter, since at these wavelengths we usually do not have the resolution to disentangle between bulge and disk.

2.7 Generating sky positions

The final step is to generate a position on the sky for each galaxy. Here we make very simplistic assumptions. First, we assume the same angular correlation at all redshifts, which means that galaxies

will be clustered on the same angular scale. This angular scale will correspond to a smaller proper distance at $z = 0.5$ than at $z = 1$, so it will somehow mimic the increase of proper distance clustering with time. Second, we consider that there is no sub-population of galaxies that is more clustered than the rest. E.g., massive early-type galaxies are treated the same way as dwarf star-forming galaxies. While this is probably wrong, it should be a sufficient approximation for now, and we can easily improve this later if need be. In fact, clustering is a relatively minor ingredient, and for our purposes it is only important that we generate catalogs with realistic sky-projected galaxy densities, with voids and peaks. The dependence on galaxy colors and properties is a second order effect.

We use these assumptions to measure the correlation function in the real GOODS–South catalog. We take into account that this correlation function is blurred by photometric redshift uncertainties, and use it to generate the position of each galaxies within a given redshift slices in the mock catalog using the Soneira & Peebles algorithm (power law index equal to 0.4, number of levels $N_{\text{level}} = 4$). Doing so, one gets the right two-point correlation slope, but not the right amplitude: the correlation is too strong at all scale. To fix this, one has to say that there is a fraction (60%) of the sample which is not clustered, and we assign them uniformly random sky positions. This way, we reproduce the observed two-point correlation function over the whole field.

3 Results

We use two diagnostics to assess the quality of this mock catalog in each photometric band. The first one is the flux distribution of all galaxies, and the second is the pixel distribution of simulated images (only for confused FIR images where blending is important).

In what follows, we use a mock catalog generated with 90% completeness in H -band down to $H = 29$, from $z = 0.01$ to $z = 6$. Over 17×17 arcmin, this represents 104 000 galaxies. The minimum stellar mass goes as low as $5 \times 10^4 M_{\odot}$ at $z = 0.01$, and rises with redshift to reach $7 \times 10^6 M_{\odot}$ at $z = 1$, and $10^8 M_{\odot}$ at $z = 4$.

3.1 Optical magnitudes

Fig. 3 is showing the agreement of the total magnitude distribution, in multiple bands. This agreement is very good in the NIR. Since these wavelengths are most closely correlated to the stellar mass of the galaxies, and since the mock catalog was built to reproduce exactly the stellar mass function in GOODS–South, this should not come as a surprise. Still, this shows that the procedure works well. Generating the UV-optical (F435W and F606W) fluxes is more complex, because these bands actually trace the emerging UV light coming from star formation. Nevertheless, the agreement here is also very good.

We quantify the differences using the χ^2 statistics, and assuming only Poisson uncertainties (i.e., statistical fluctuations in the histograms, but not flux measurement uncertainties). For each of these bands, we measure reduced χ^2 of, respectively (from top-left to bottom-right), 4.23, 3.66, 2.22, 3.75, 2.31 and 8.20 (for magnitudes brighter than 27, 27, 26, 26, 25 and 25, respectively). If our simulation was a perfect match to the data, and the observed differences were only due to statistical fluctuations, we would obtain $\chi^2 \sim 1$. The fact that we do not reach this value indicates that there are, of course, more subtle mechanisms in the real Universe than what we introduced here. In particular, the χ^2 of the IRAC channel 4 magnitudes is particularly high. We suspect this is due to the peculiar position of the observed $8 \mu\text{m}$, which is probing dust emission at low-redshifts, and stellar emission at higher redshifts. The simulation here can be improved by introducing a better treatment of the junction point between these two wavelength regimes, and by choosing more carefully the IR SED. This is currently work in progress.

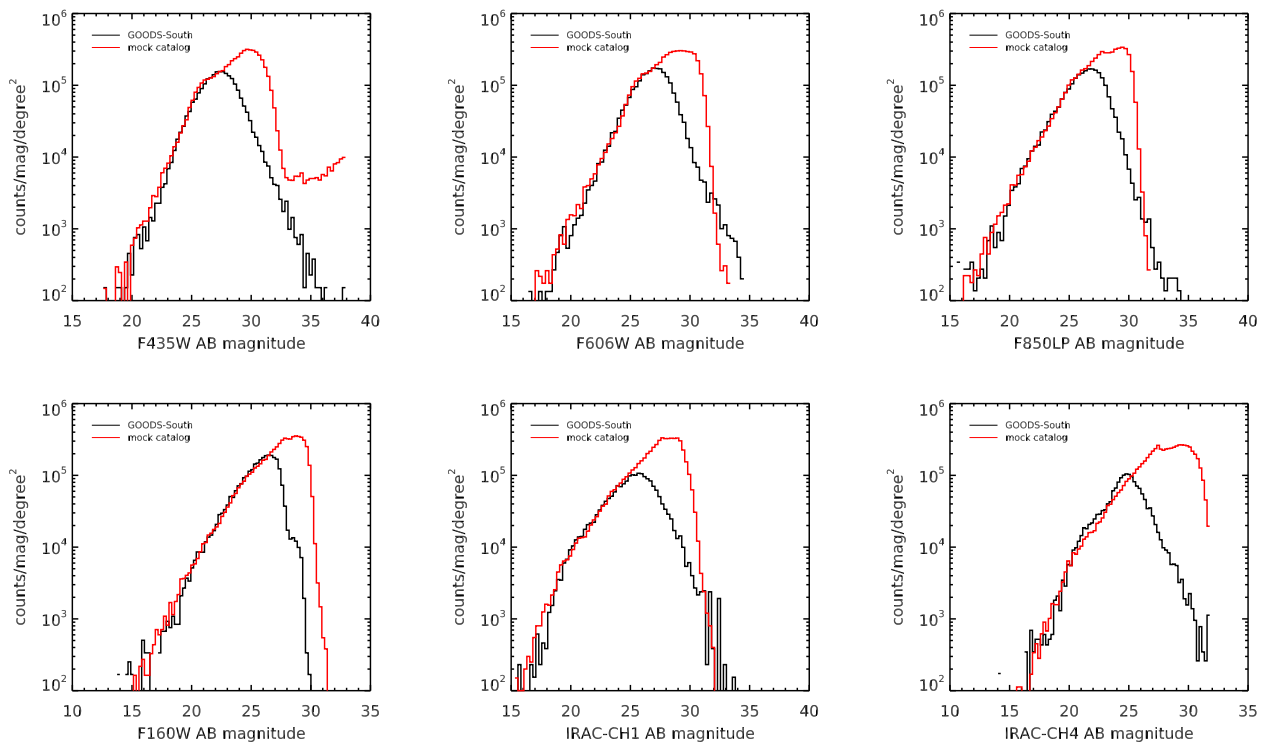


Figure 3: Total magnitude distribution of the real GOODS–South catalog (black) and the mock catalog (red), in different *HST* bands and *Spitzer* IRAC.

3.2 FIR fluxes

Fig. 4 shows the same plots, this time with the FIR fluxes. Again, the agreement is excellent. The χ^2 values are, respectively, 4.29, 2.25, 1.65, 1.10, 0.47, 1.50. Because the available observations are less extensive than for the optical magnitudes, these χ^2 are less stable, but still we do find values very close to 1. The worst case is that of the MIPS $24\mu\text{m}$, which is likely related to the IRAC $8\mu\text{m}$ issue we reported in the previous section.

We also analyze in Fig. 5 the pixel histogram distribution of the simulated maps against the observed maps. This second test is important because of the blending, which sometimes pollutes the measured flux catalogs (two sources are combined into a single one), which tends to produce more bright fluxes than there actually is in the real Universe. By analyzing the map statistics directly, one gets rid of this issue of the counter part identification. This comparison also takes into account the clustering, which will tend to increase the contrast of the map without actually changing the fluxes of individual galaxies. The downside is that the bright pixel counts are very sensitive to statistical fluctuations, and a single very bright (but usually rare) object can drastically impact the measured distribution. Yet, here also the agreement is good. We find $\chi^2 = 3.03, 1.47, 4.98, 3.28, 2.71,$ and 1.09 .

3.3 Generate images

Finally, we give an example is the simulated images we have produced in Fig. 6. This illustrates the power of our simulations, which are now physically consistent from the UV to the far-IR.

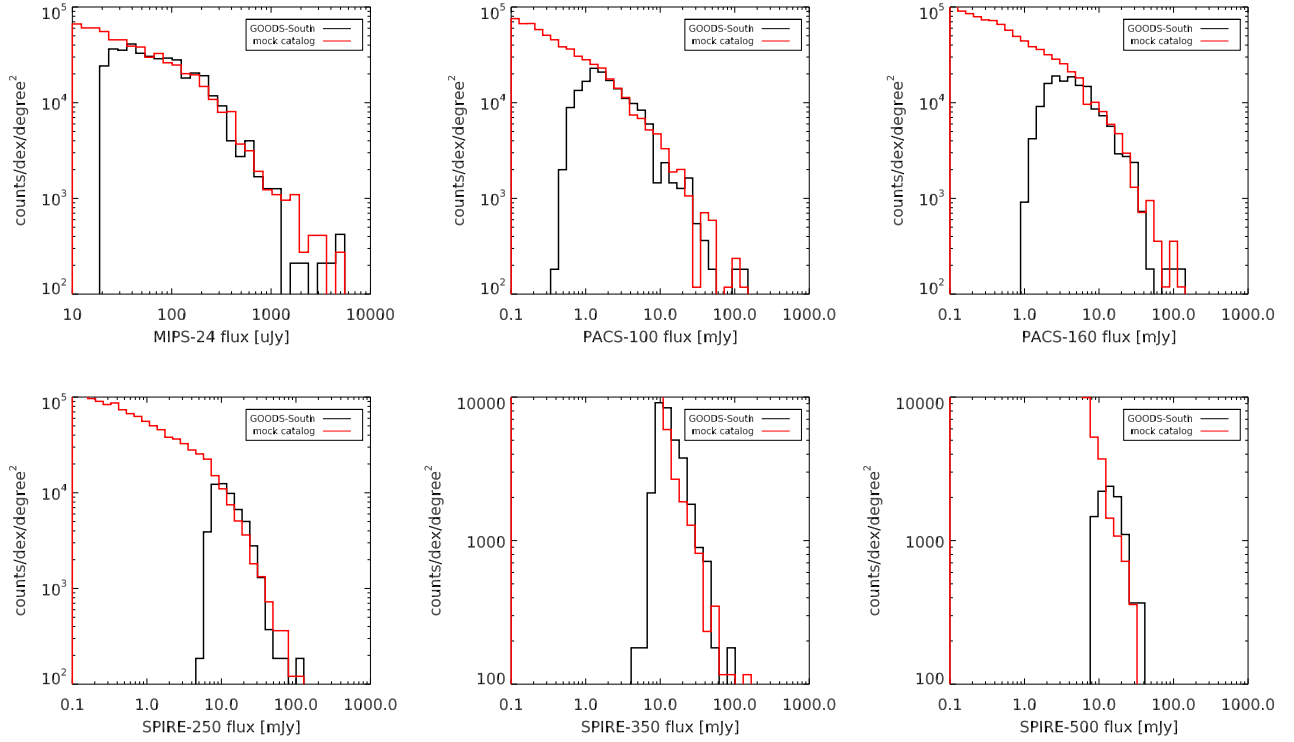


Figure 4: Total flux distribution in the MIR to FIR of the real GOODS–South catalog (black) and the mock catalog (red).

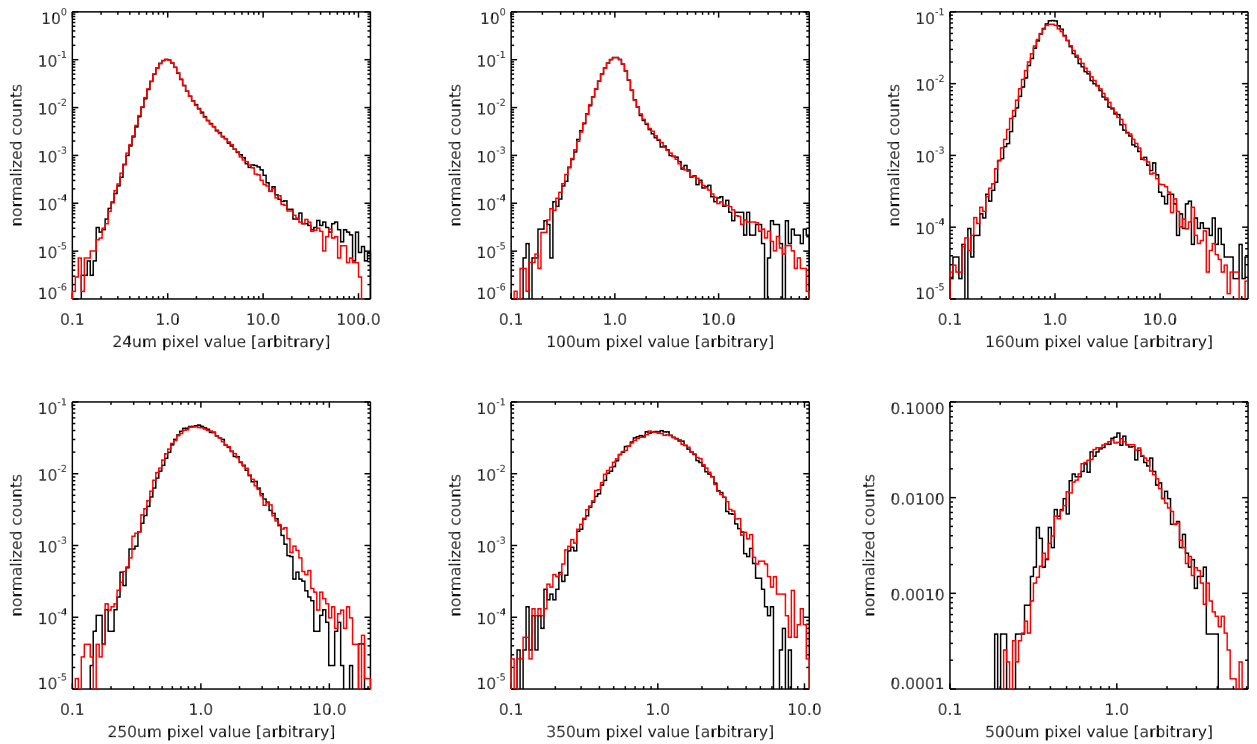


Figure 5: Pixel histogram distribution of the simulated FIR images versus real images in GOODS–South.

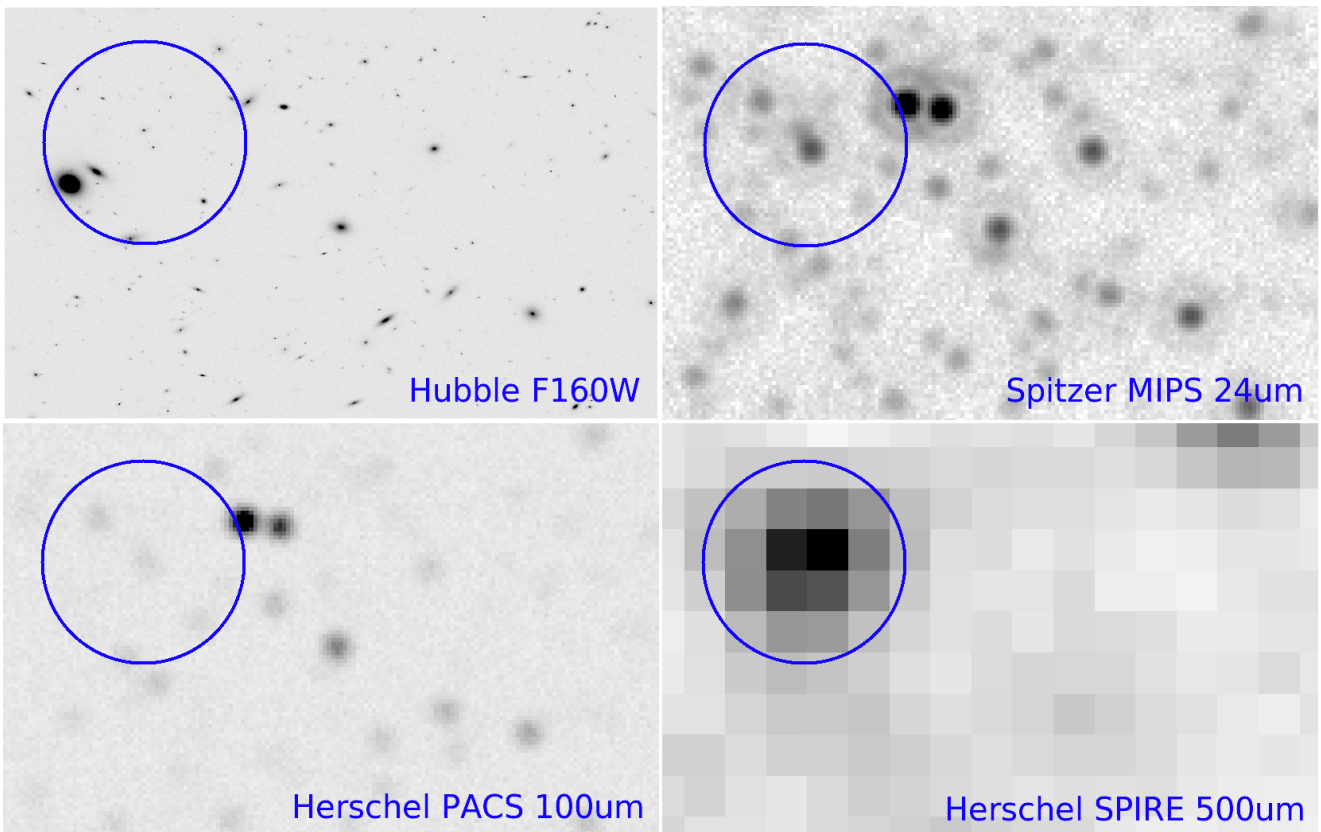


Figure 6: Simulated maps in the *Hubble* H band (top-left), *Spitzer* 24 μm (top-right), *Herschel* PACS 100 μm (bottom-left) and SPIRE 500 μm (bottom-right).

Simulating images using Gencat mock catalogues

To generate images starting from Gencat catalogues we used E. Bertin's software SkyMaker, which produces realistic simulated images including sources and a (non-correlated) noise map. We wrapped SkyMaker into an ad-hoc user friendly Python script, to control all parameters with ease.

In summary, the procedure is as follows:

- the catalogues list positions and structural parameters of sources in a given band
- SkyMaker reads such list and produces an image based on it, requiring the following additional parameters (to be given in a config file):
 - image size in pixels;
 - gain;
 - saturation level;
 - exposure time;
 - magnitude zero point;
 - pixel size;
 - seeing FWHM;
 - simulated optical instrument features (mirrors diameter, etc.);
 - background magnitude per arcsecond;
 - limit of allowed magnitudes.

Some of these parameters are kept fixed: e.g, all images have dimensions of 16500x16400 pixels, with allowed magnitudes 16 to 31, the gain is assumed to be 1, all images have pixels size $ps=0.06''$ and the saturation level is 6553500 counts/s. The photometric zero point is fixed to 23.9.

Fixing the exposure time to 10000 sec for all images, the only free parameter is the background magnitude. However, it is easier to input a magnitude limit e.g. at 1σ , which can be taken as equal to the ones obtained for the CANDELS observations, and hence compute the background magnitude for the simulated images. To do so, we start from the formula:

$$\frac{S}{N} = \frac{(F_1 t_{\text{exp}})}{\sqrt{\frac{F_1 t_{\text{exp}}}{g} + \frac{B_1 t_{\text{exp}} A}{g} + (R.O.N./g)^2}}$$

where F_1 is source flux in counts/s, B_1 is background flux in counts/s, A is pixel area of the source, and g is gain, which is fixed to 1. Assuming the R.O.N. to be zero, a source of magnitude equal to $\text{mag}_{\text{limit}}$ has $S/N=1$ yielding:

$$1 = \frac{F_1 t_{\text{exp}}}{\sqrt{(F_1 + B_1 A) t_{\text{exp}}}} \quad \text{and therefore} \quad B_1 = \frac{F_1^2 t_{\text{exp}} - F_1}{A} \quad \text{where } F_1 = 10^{-0.4(\text{mag}_{\text{limit}} - ZP)}$$

$$\text{from which } \text{mag}_{\text{background}} = -2.5 \log \frac{B_1}{PS^2} + ZP$$

The limit magnitudes in 1 FWHM for all bands were computed from the nominal ones given in Guo et al. 2014, as $m_{\text{limit}} = m_{1\sigma} = m_{5\sigma, \text{CANDELS}} + 2.5 \log 5$, with minor adjustments for "cosmetics":

VIMOS_U=29.5 (true: 29.72), ACS_f435=30.5 (true: 30.70), ACS_f606=30.5 (true: 31.10), ACS_f775=30.5 (true:30.30), ACS_f814=30.5 (true:30.60), ACS_f850=30.5 (true: 30.30), WFC3_f105=29.25 (true: 29.20), WFC3_f140=29.25 (true: 29.40), WFC3_f160=29.25 (true: 29.11), K_Hawki=28.2 (true: 28.20), IRAC1=27.15 (true: 27.15), IRAC2=27.15 (true: 27.15), IRAC3=25.5 (true: 25.50), IRAC4=25.5 (true: 25.47).

FWHM were taken as follows:

VIMOS_U=0.8", ACS_f435=0.1", ACS_f606=0.1", ACS_f775=0.1", ACS_f814=0.1", ACS_f850=0.1", WFC3_f105=0.2", WFC3_f140=0.2", WFC3_f160=0.2", K_Hawki=0.4", IRAC1=1.66", IRAC2=1.7", IRAC3=1.9", IRAC4=2.0".

The Python script we developed to produce the images calls SkyMaker iteratively to produce a set of ancillary files, i.e. a normalized image with pixels values in counts/s, a normalized and background subtracted image (obtained using the "true" background value computed as explained above), an RMS image obtained computing the standard deviation of the pixel values in the noise map image (no photon noise is therefore included).

To produce the images, SkyMaker needs a PSF. It can be generated internally, or it can be fed to the code as an external file. Internally generated PSFs have perfect circular symmetry. We used internally generated PSFs for all bands but for the four IRAC ones, because of the intrinsic asymmetry of the real IRAC PSFs. For IRAC images we therefore fed SkyMaker with "realistic" synthetic IRAC PSFs generated using a Python script by the H. Ferguson and S. Lee (CANDELS). Below, in Fig.7 and Fig.8, we show examples of the used PSFs and the resulting simulated images in all bands and different magnifications.

Simulated datasets can be found in:

<ftp://ftp.astrodeep.eu/SIMULATIONS/gencat/images/> (passwd protected).

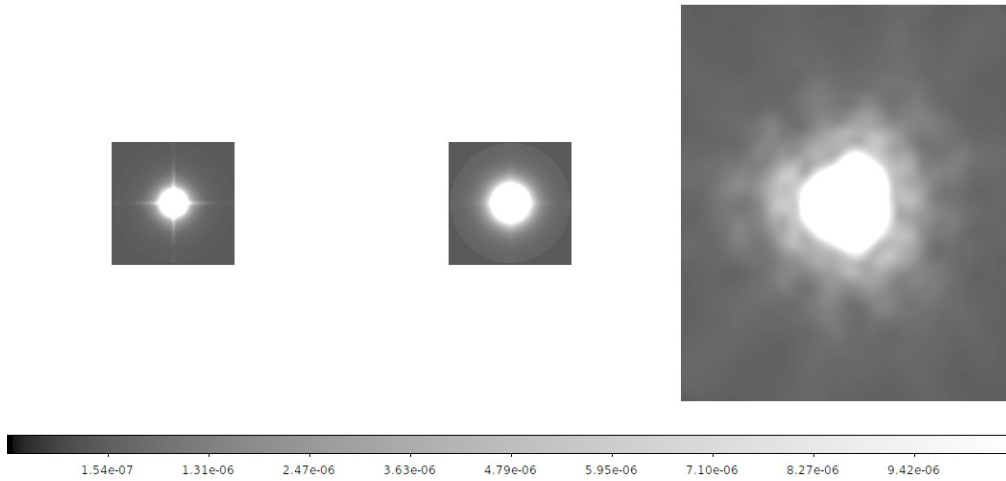


Figure 7: Three of the adopted PSFs. Left to right: *WF3_f160*, *K_Hawkl*, *IRAC1*.

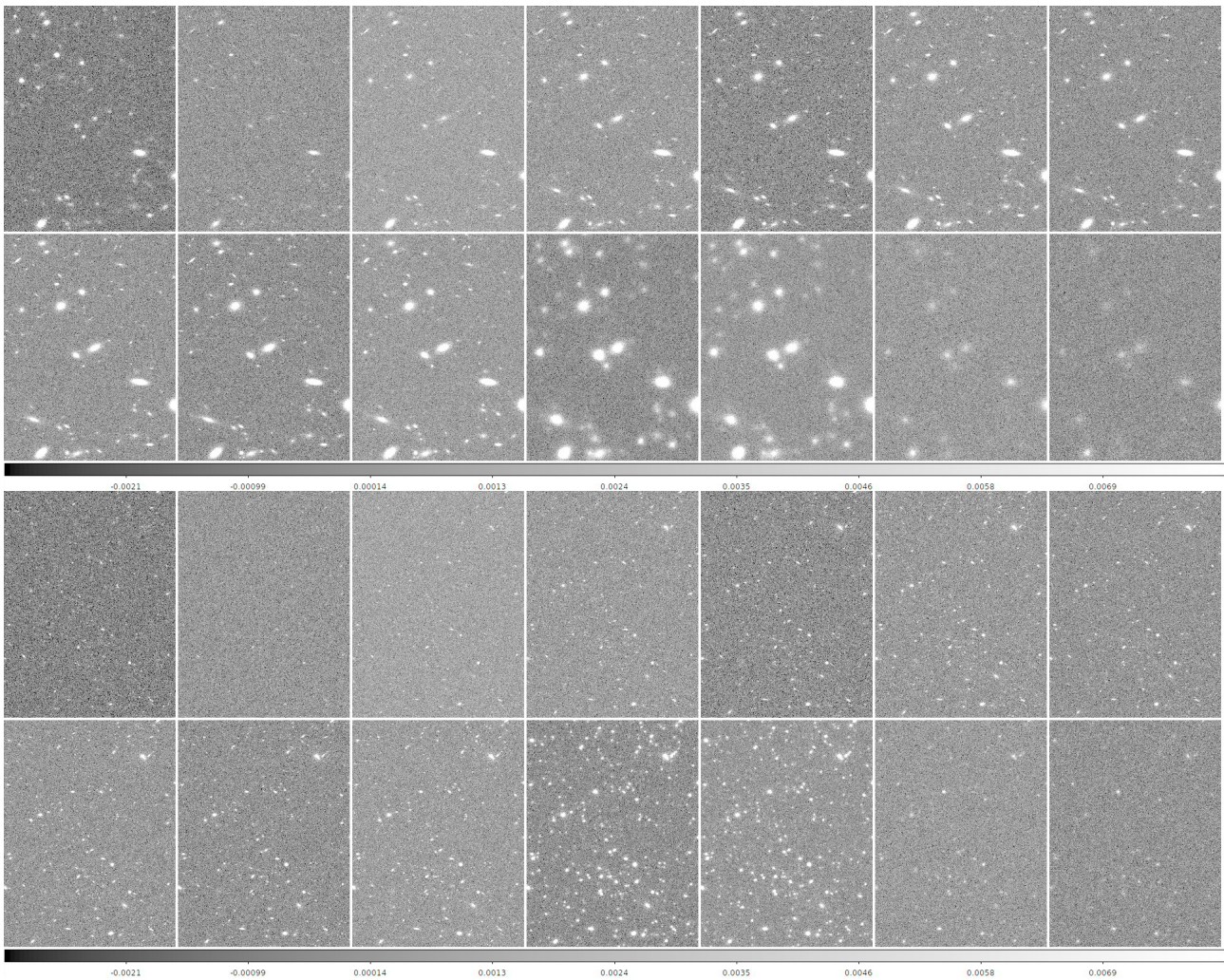


Figure 8: Regions within simulated images at different magnifications. Both panels, left to right, top to bottom: *VIMOS_U*, *ACS_f435*, *ACS_f606*, *ACS_f775*, *ACS_f814*, *ACS_f850*, *WFC3_f105*, *WFC3_f140*, *WFC3_f160*, *K_Hawkl*, *IRAC1*, *IRAC2*, *IRAC3*, *IRAC4*.